

tRNA tracking for direct measurements of protein synthesis kinetics in live cells

Ivan L. Volkov^{1,2}, Martin Lindén^{1,2}, Javier Aguirre Rivera¹, Ka-Weng leong¹, Mikhail Metelev¹, Johan Elf¹ and Magnus Johansson^{1*}

Our ability to directly relate results from test-tube biochemical experiments to the kinetics in living cells is very limited. Here we present experimental and analytical tools to directly study the kinetics of fast biochemical reactions in live cells. Dye-labeled molecules are electroporated into bacterial cells and tracked using super-resolved single-molecule microscopy. Trajectories are analyzed by machine-learning algorithms to directly monitor transitions between bound and free states. In particular, we measure the dwell time of tRNAs on ribosomes, and hence achieve direct measurements of translation rates inside living cells at codon resolution. We find elongation rates with tRNA^{Phe} that are in perfect agreement with previous indirect estimates, and once fMet-tRNA^{fMet} has bound to the 30S ribosomal subunit, initiation of translation is surprisingly fast and does not limit the overall rate of protein synthesis. The experimental and analytical tools for direct kinetics measurements in live cells have applications far beyond bacterial protein synthesis.

Since dawn of molecular biology, the reductionist's approach has guided researchers to dissect the complexity of living systems into separately measurable units. In vitro reconstituted systems have been successfully exploited to deduce molecular mechanisms of the central biochemical pathways that are fundamental to all life forms. However, studying a molecular mechanism separately in isolated systems is not always sufficient. The cellular machineries work together in a finely tuned coalition, and the complexity of interactions is difficult to mimic in reconstituted systems because of macromolecular crowding, geometrical constraints, and our limited understanding of the detailed chemical composition at the single-cell level. Studies of dynamic molecular processes directly inside the cell have also been challenging. Though classical test-tube biochemistry has relied on tricks to synchronize the binding state of reacting molecules for kinetics measurements, this is difficult, if not impossible, to accomplish in a living cell, wherein reactions are asynchronous and normally work under steady state conditions. With the development of single-molecule approaches, the need to synchronize the molecules in the system of interest disappears, and in vivo reaction kinetics measurement should in principle be attainable.

Recent advances in the field of single-molecule fluorescence microscopy have opened up the possibility to probe molecular interactions directly inside cells. These studies commonly depend on fluorescent fusion proteins because of their genetically encoded specificity and ease of use. Tracking of individual fluorescent fusion proteins has, for example, helped in determining the fractions of proteins that are in different binding states and how these different complexes are distributed in the cells¹. However, to measure the rates of binding and dissociation reactions inside the cells by single-molecule tracking, it is necessary to detect the corresponding changes in the diffusion rate for individual molecules. Moreover, to reliably assign dwell times for different diffusional states, one would need sufficiently long and highly resolved trajectories to observe the fluorophores through a whole reaction cycle. This has, to a limited extent, been possible with fluorescent protein labels² but would be very difficult to generalize for reaction pathways involving several

diffusional states or different timescales because of the modest photon budget of the fluorescent proteins³.

Recently, Kapanidis and co-workers demonstrated how in vitro dye-labeled molecules could be introduced to live cells using conventional electroporation techniques^{4,5}. This methodology opens the possibility to use synthetic dyes for site-specific labeling of biomolecules to be studied in vivo. Because of their small size, the dyes make very gentle perturbations to the target molecules, and their superior photophysical properties make their potential as tools for in vivo single-molecule tracking encouraging.

Bacterial protein synthesis is a typical example of a complex biological process. Protein synthesis has been studied extensively over the years, and the combination of traditional biochemistry^{6–8}, structural approaches^{9–11}, and more recently single-molecule-based in vitro techniques^{12,13} has led to a detailed picture of ribosome-catalyzed protein synthesis¹⁴. However, to connect this detailed picture with cell physiology, new techniques are needed to probe the dynamics of these processes inside the cell. In particular, the kinetics of the highly regulated steps of translation initiation have proven very difficult to disentangle using reconstituted systems. For example, the time for 50S subunit joining to the fMet-tRNA^{fMet}·30S-mRNA pre-initiation complex varies 100-fold in vitro depending on concentrations of the individual initiation factors, whereby both low and high factor concentrations impede the process^{15,16}. In the present study, we have developed experimental and analytical tools to directly measure biochemical reaction rates inside living cells. We apply this method to protein synthesis and use electroporated dye-labeled tRNAs to extract quantitative kinetic data from protein synthesis with codon resolution inside live cells.

Results

Efficient electroporation of dye-labeled tRNA. In vitro-labeled and assayed Phe-[Cy5]tRNA^{Phe} (Supplementary Fig. 1) was introduced into DH5α *Escherichia coli* cells by electroporation. After recovery, cells were plated on an agarose pad and imaged at 37°C (Fig. 1a). At 19kV/cm electroporation field strength and 100nM

¹Department of Cell and Molecular Biology, Uppsala University, Uppsala, Sweden. ²These authors contributed equally: Ivan L. Volkov, Martin Lindén. *e-mail: m.johansson@icm.uu.se

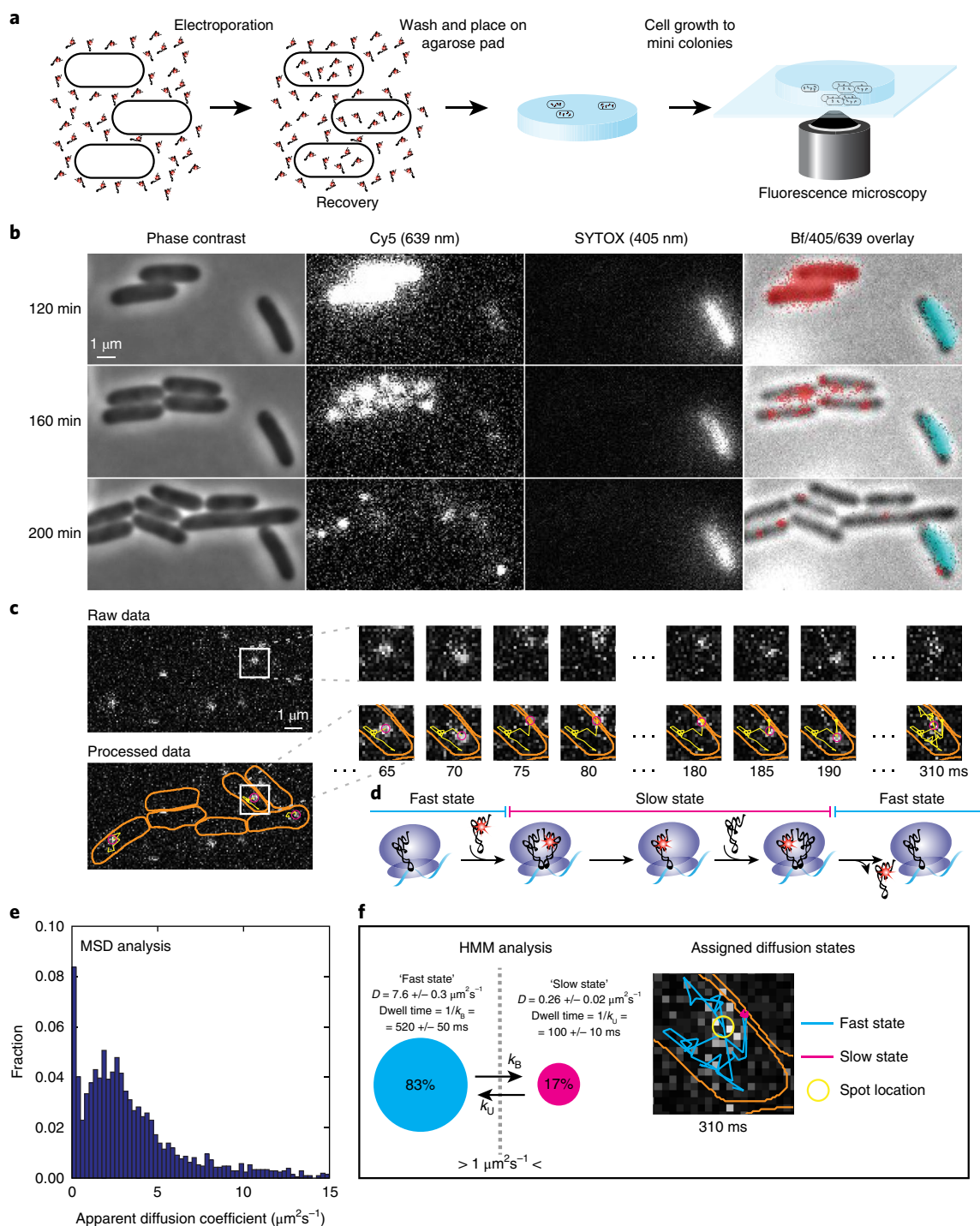


Fig. 1 | Tracking of single [Cy5]tRNA^{Phe} in live *E. coli* cells. **a, *E. coli* cells were electroporated with Phe-[Cy5]tRNA^{Phe}, recovered in RDM (rich defined medium), washed and placed in dilute culture on an RDM-agarose pad, and allowed to grow to mini colonies before data acquisition. **b**, Phase-contrast, fluorescence, and bright-field (Bf) imaging of cells after electroporation with Phe-[Cy5]tRNA^{Phe}. [Cy5]tRNA^{Phe} appear as bright pixels in the Cy5 lane and red pixels in the overlay lane. SYTOX stained, i.e., dead cells (bright pixels in the SYTOX lane and cyan pixels in overlay lane), were omitted in the analysis. Live cells continued growing after laser exposure during data acquisition (Supplementary Fig. 2). **c**, Time series of tRNA tracking at 5 ms per frame showing cell outlines (orange), present location of the particle (magenta), and the particle trajectory over time (yellow). This example shows an apparent binding of approximately 100 ms. Scale bar, 1 μm . **d**, Predicted diffusion of [Cy5]tRNA^{Phe} molecules being used on ribosomes. **e**, Histogram of apparent diffusion coefficients for [Cy5]tRNA^{Phe} in live *E. coli* cells, estimated from mean-squared displacement (MSD) analysis of trajectories such as that in **c**. **f**, HMM-estimated diffusion of [Cy5]tRNA^{Phe} in live *E. coli* cells, coarse-grained from a six-state model (Supplementary Table 1) into two states, 'slow' and 'fast', with a threshold of $1 \mu\text{m}^2/\text{s}$ separating them. The right part shows the trajectory in **c**, now color coded with respect to diffusional state. 17,286 total time steps were included in the analyses in **e** and **f**.**

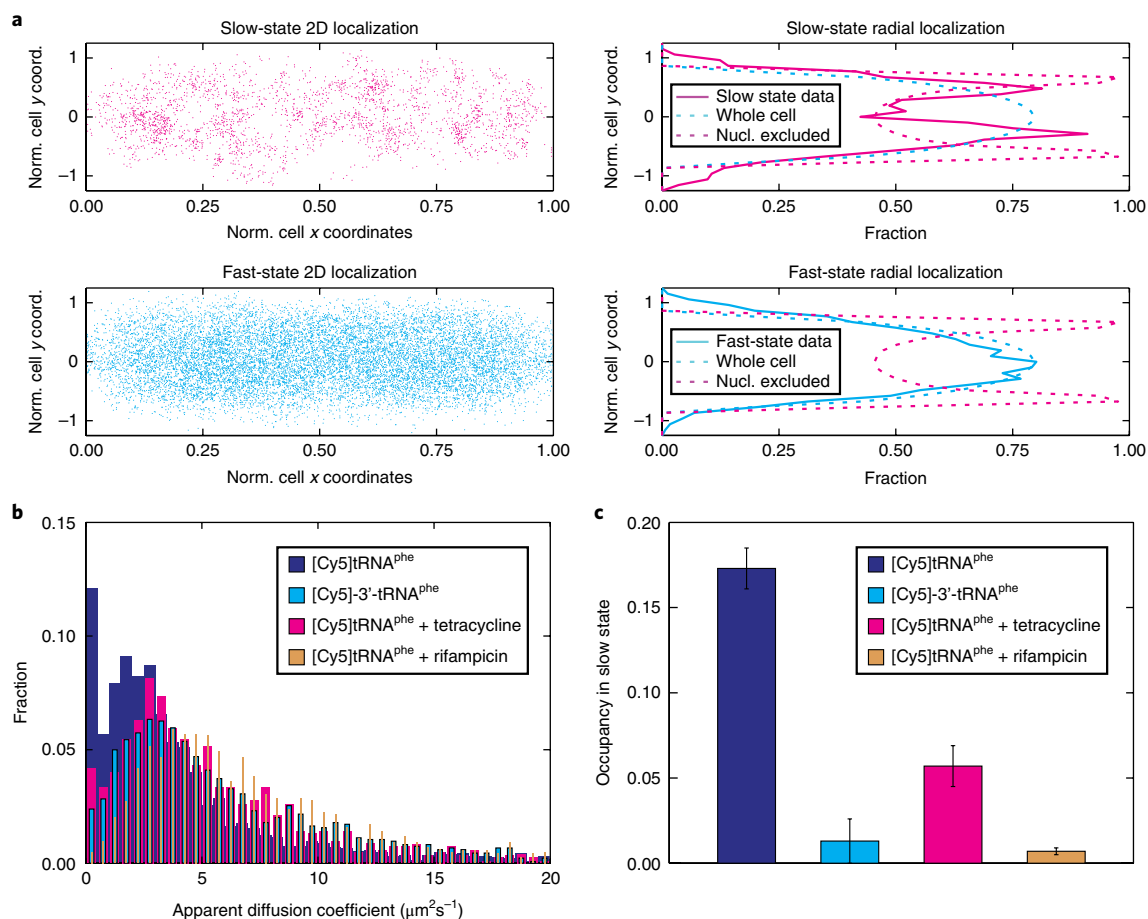


Fig. 2 | Internalized [Cy5]tRNA^{Phe} takes an active part in translation. **a**, Spatial distribution of [Cy5]tRNA^{Phe} in DH5α cells belonging to the slow or the fast diffusive state according to coarse-grained HMM analysis ($n=17,286$). In the left panels, locations are plotted on normalized cell width (y , -1 to 1) and length (x , 0 to 1) coordinates. The right panels show the same data (excluding particles in cell poles and the cell center; i.e., including particles within $0.2 < x < 0.4$ or $0.6 < x < 0.8$) projected on the short cell radial axis (solid lines). Dashed lines correspond to uniform distributions in the cytoplasm and nucleoid excluded regions. **b**, MSD-estimated apparent diffusion coefficients of 3' inactivated tRNA (3'-[Cy5]tRNA^{Phe}, $n=11,231$) in live *E. coli* cells, as well as normal [Cy5]tRNA^{Phe} in mini colonies of *E. coli* cells treated with tetracycline ($n=10,415$) or rifampicin ($n=12,042$). Data for [Cy5]tRNA^{Phe} in nontreated cells are shown for comparison. **c**, HMM-estimated occupancy of the dye-labeled tRNAs in the slow diffusive state (see Supplementary Table 1). The trajectories used were the same as those in **b**. Error bars represent bootstrap estimates of standard error.

Phe-[Cy5]tRNA^{Phe}, approximately 10% of the cells resume growth and division on the pad and about 70% of those have internalized [Cy5]tRNA^{Phe}, with an average number of 80 fluorescent molecules per cell (Supplementary Note). The fluorescent molecules are stable inside the cells, with no obvious decay on the hour timescale, and are distributed equally between daughter cells upon cell division (Fig. 1b). In all electroporation experiments presented below, the procedure includes growth from single cells to mini colonies (four to eight cells per colony) on the pads before fluorescence movie acquisition. To exclude single dead cells, the pads also contained SYTOX blue, selectively staining dead cells with damaged membrane (Fig. 1b).

Tracking of single fluorescent tRNAs inside live cells. To detect and track the movement of individual internalized [Cy5]tRNAs, we used stroboscopic laser illumination with 1.5 ms laser illumination per 5 ms camera exposure frame. Combining symmetry-based spot detection¹⁷, maximum a posteriori estimates of position and localization uncertainty¹⁸, and the u-track algorithm¹⁹, we were able to follow the movement of single [Cy5]tRNA^{Phe} (Fig. 1c) up to more than 100 frames (See Supplementary Fig. 3a–c for detection results). As shown in Supplementary Video 1 and Fig. 1c, the internalized

Cy5-labeled tRNAs display diffusion patterns consistent with what would be expected for a tRNA being used repeatedly by the protein synthesis machinery, i.e., random fast diffusion interrupted by immobilization events, possibly reporting on binding of the tRNAs to an mRNA-tethered ribosome (Fig. 1d).

Further, the apparent diffusion coefficients of the tRNAs, estimated from mean-squared displacement (MSD) plots of trajectory segments, show a wide distribution of fast-moving tRNAs, with the apparent binding events giving rise to a population (12%) with apparent diffusion $< 0.5 \mu\text{m}^2/\text{s}$ (Fig. 1e), potentially representing ribosome-bound tRNA^{1,20}. The diffusion pattern is robust between independent experiments (Supplementary Fig. 3d), and all data analyses in this study were therefore performed on cumulated data from independent experiments (two or more), with sample size n denoting the total combined number of trajectory time steps in the analysis.

To quantify binding events in terms of the accompanying changes in diffusion constant, we used a hidden Markov model (HMM) approach, which models the trajectories as random (Markovian) transitions between a set of discrete (hidden) states with different diffusion constants, accounts for point-wise localization errors and motion blur, and learns the underlying sequence of state transitions

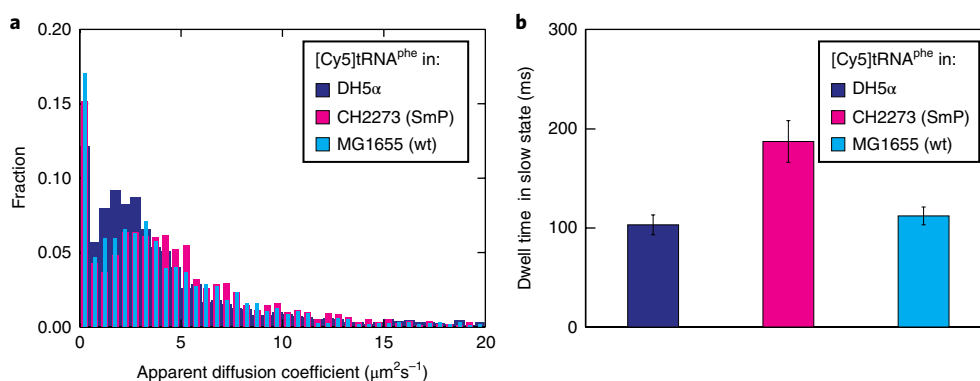


Fig. 3 | [Cy5]tRNA^{Phe} dwell time is longer on slow ribosomes. a, MSD-estimated apparent diffusion coefficients of [Cy5]tRNA^{Phe} in streptomycin pseudodependent CH2273 cells (SmP, $n=15,571$) and the CH2273 genetic background strain MG1655 ($n=10,239$). Data for [Cy5]tRNA^{Phe} in DH5 α cells (Fig. 1e) are shown for comparison. **b**, HMM-estimated dwell times for [Cy5]tRNA^{Phe} in the slow state (see Supplementary Table 1). The trajectories used were the same as those in **a**. Error bars represent bootstrap estimates of standard error.

from data. The HMM algorithm performs maximum-likelihood inference of model parameters¹⁸, and we used Akaike's information criterion²¹ (AIC) to determine the appropriate number of diffusive states to fit the data. For models of four states and more, we consistently found three major diffusive states at approximately $0.1 \mu\text{m}^2/\text{s}$, $3 \mu\text{m}^2/\text{s}$, and $6 \mu\text{m}^2/\text{s}$, with corresponding approximate occupancies at around 15%, 50%, and 20%, respectively (see Supplementary Fig. 3f and Supplementary Table 1 for the six-state model, with lowest AIC). With an increasing number of states, we found low occupancy (<5%) states at $0.7 \mu\text{m}^2/\text{s}$ and $5 \mu\text{m}^2/\text{s}$. In addition, for all model sizes we detected one or two states with significantly faster diffusion $>20 \mu\text{m}^2/\text{s}$. Based on our analysis of simulated microscopy images (below), we believe these $>20 \mu\text{m}^2/\text{s}$ states reflect tracking artifacts with no biological meaning. Considering that the intracellular concentration of elongation factor Tu (EF-Tu) roughly equals that of total tRNA²², and that approximately 75% of tRNA^{Phe} is aminoacylated during exponential growth^{23,24}, we tentatively assigned the three major states as a [Cy5]tRNA^{Phe}-70S-mRNA complex, [Cy5]tRNA^{Phe} in ternary complex with EF-Tu and GTP, and a free [Cy5]tRNA^{Phe}. Tracking of a fluorescent fusion version of EF-Tu performed with similar experimental settings yielded a major (>75% occupancy) diffusional state at around $3 \mu\text{m}^2/\text{s}$ (Supplementary Table 1), supporting the assignment of the $3 \mu\text{m}^2/\text{s}$ tRNA diffusional state as the ternary complex.

All experimental data sets presented in this article were fitted to two-, seven-, or eight-state models, and the best models (lowest AIC) are shown in Supplementary Table 1. As the aim of the present study regards ribosome binding events, however, we coarse-grained the best HMM fits into two states, 'slow' and 'fast', with a threshold of $1.0 \mu\text{m}^2/\text{s}$ separating them (Fig. 1f and Supplementary Fig. 3f), in line with MSD analysis of ribosome trajectories performed in refs 1,20,25. The corresponding coarse-grained results for all experiments are shown in Supplementary Table 1, and our main focus in the following sections will be the slow state. An example of tracked molecules with HMM-fitted diffusional states is shown in Supplementary Video 1.

Internalized fluorescent tRNAs take part in translation. We next sought to evaluate whether the apparent [Cy5]tRNA^{Phe} binding events actually represent binding to ribosomes. We first note that [Cy5]tRNA^{Phe} molecules in the slow diffusional state are located more toward the cell periphery compared to [Cy5]tRNA^{Phe} in the fast state (Fig. 2a). Considering that ribosomes in growing cells are primarily excluded from the nucleoid in the center of the cells^{1,20}, peripheral slow movement of [Cy5]tRNA^{Phe} fits well with

the hypothesis that the slow state represents ribosome-bound [Cy5]tRNA^{Phe}.

In an attempt to specifically remove the [Cy5]tRNA^{Phe} association to ribosomes, cells were subjected to the antibiotics rifampicin or tetracycline. Rifampicin inhibits RNA transcription, and hence when all mRNAs have been degraded no further translation can occur and there should be no functional binding of [Cy5]tRNA^{Phe} to ribosomes. Tetracycline, on the other hand, binds directly to the ribosome, where it is believed to block binding of the aminoacyl (aa)-tRNA-EF-Tu-GTP ternary complex to the A site, resulting in ribosomes being trapped at start codons²⁶. After antibiotic injection, both MSD analysis (Fig. 2b) and diffusion-state analysis using the HMM approach (Fig. 2c and Supplementary Table 1) clearly show a decrease in binding events in the presence of either of the drugs—the occupancy in the slow state decreases from 17% to 1% and 6%, respectively.

By tracking 3' deactivated [Cy5]-3'-tRNA^{Phe}, we also found fewer binding events (1% occupancy in slow state), further supporting the idea that the internalized normal [Cy5]tRNA^{Phe} takes part in protein synthesis on ribosomes (Fig. 2b,c).

In vivo kinetics of translation elongation. Under the assumption that the slow diffusional state of the [Cy5]tRNA^{Phe} represents productive tRNA usage on ribosomes, the apparent binding events allow a direct measure of mRNA translation kinetics in vivo. With rapid dissociation of deacylated tRNA from the E site²⁷, one binding event would represent the total time of two consecutive elongation steps, i.e., two peptide bond formation steps, two translocation steps, plus one aa-tRNA-EF-Tu-GTP ternary complex arrival time (Fig. 1d). We estimated the dwell times of the [Cy5]tRNA^{Phe} in the different diffusional states based on the transition matrix of the coarse-grained two-state HMMs and found the mean dwell time of [Cy5]tRNA^{Phe} on ribosomes to be 100 ± 10 ms (Supplementary Table 1).

The resulting [Cy5]tRNA^{Phe} dwell time on ribosomes fits very well with previous in vivo estimates of the average elongation rate, which is approximately 50 ms per amino acid incorporated at 37°C ²⁸; in vitro biochemical measurements performed in reconstituted protein synthesis systems²⁹, as well as analysis of the expected tRNA^{Phe} utilization frequency at this growth rate (Supplementary Note).

To further validate our in vivo kinetics assay, we used an *E. coli* strain (CH2273) with a well-characterized streptomycin pseudodependent phenotype, SmP, harboring two mutations in gene *rpsL* encoding ribosomal protein S12. The resulting mutant ribosomes are hyperaccurate, but slow^{30,31}, and therefore need the error-inducing

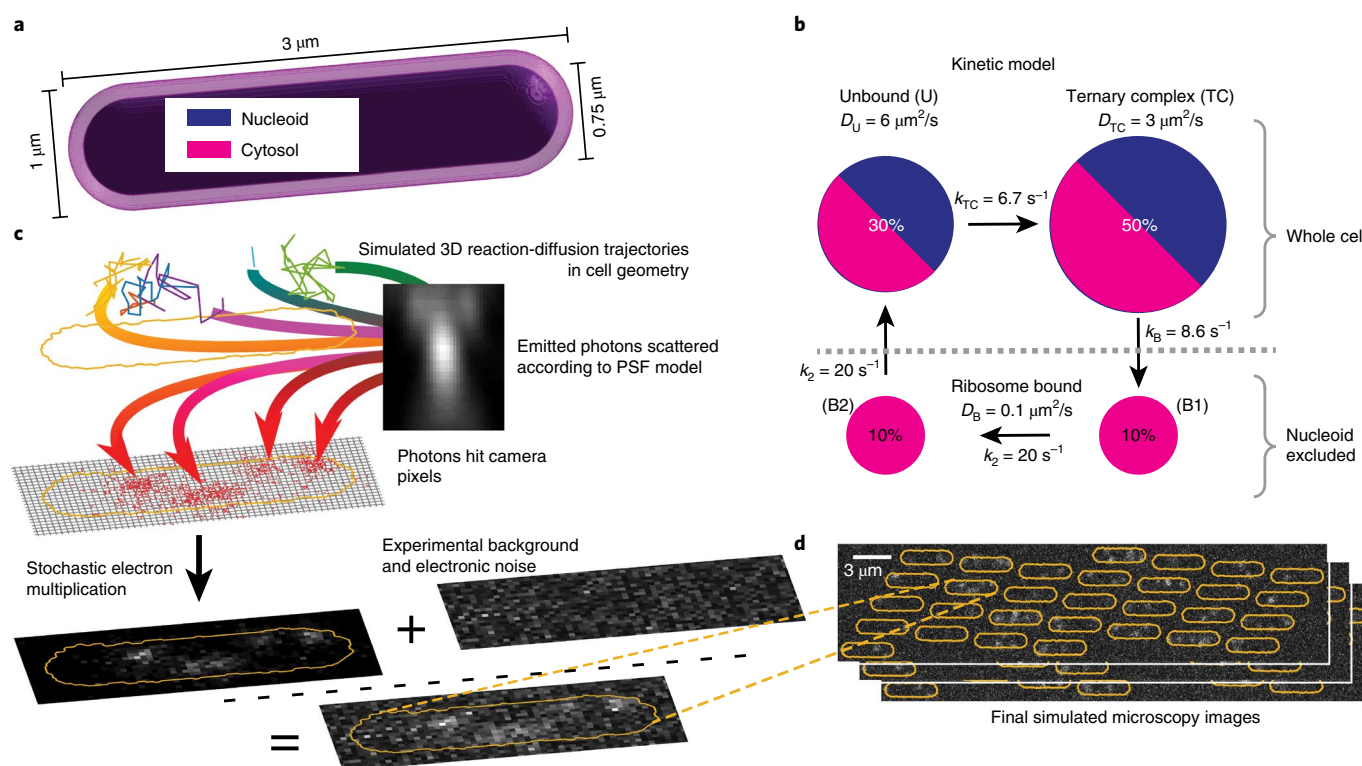


Fig. 4 | Simulated single-molecule microscopy. **a**, Model geometry for reaction-diffusion simulations of translation cycles in *E. coli*. The cytosol and nucleoid are modeled as concentric cylinders with spherical end caps. **b**, tRNA kinetic reaction cycle. Ribosome-bound states are excluded from the nucleoid, whereas the unbound and EF-Tu-bound (ternary complex) states can access the whole cell. **c**, Simulation stages for a single cell: 1–3 reaction-diffusion trajectories per cell are used as input for simulated images of moving dots; the optical and detection systems are simulated by an experimentally derived z-dependent point-spread function and EMCCD camera noise using 1.5 ms illumination in 5 ms frames as in our experiments (see Methods). Finally, experimental background images are added to produce the synthetic movie. **d**, Snapshots of a simulated field of view with 30 cells.

drug streptomycin to perform efficiently (See Supplementary Fig. 4 for growth curves). Phe-[Cy5]tRNA^{Phe} was thus electroporated into CH2273 cells, which were allowed to grow and divide in the absence of streptomycin. From both MSD (Fig. 3a) and HMM analysis (Supplementary Table 1) we found the diffusion of [Cy5]tRNA^{Phe} to be similar to that in DH5 α cells, with slow- and fast-state occupancies being practically unchanged. Importantly, however, the dwell time in the slow state, 190 ± 20 ms, is two-fold higher than that in DH5 α (Fig. 3b and Supplementary Table 1). This is in good agreement with previous measurements in vivo and in vitro, suggesting a two- to three-fold slower translation rate^{30,31}. Control experiments with the CH2273 genetic background strain (i.e., MG1655) give similar dwell times to in DH5 α (Fig. 3b and Supplementary Table 1).

Overall, the results with [Cy5]tRNA^{Phe} strongly suggest that by tracking single dye-labeled tRNAs we can measure translation kinetics with codon resolution in live cells.

Simulated microscopy validates the analysis pipeline. To investigate the precision and limitations of our single-particle tracking approach, we simulated microscopy of tRNA diffusion in cells and applied our analysis pipeline. Trajectories of single molecules, confined in a cell-shape geometry (Fig. 4a), were generated by sampling from a reaction-diffusion master equation^{32,33}. For the tRNA-ribosome interactions, we used a kinetic model with four diffusive states (Fig. 4b): two bound (B1 and B2) states (tRNA in A and P site, $D_B = 0.1 \mu\text{m}^2/\text{s}$), an unbound (U) state ($D_U = 6 \mu\text{m}^2/\text{s}$), and a ternary complex (TC) state ($D_{TC} = 3 \mu\text{m}^2/\text{s}$). Elongating ribosomes were modeled implicitly by excluding the bound states from the nucleoid region. The states interconvert via a unidirectional reaction

cycle (Fig. 4b), with reaction rates chosen so that the total mean dwell time of the bound states is 100 ms and the total occupancy is 20%, 30%, and 50% for the bound, unbound, and ternary complex states, respectively, in accordance with our experimental results (Supplementary Fig. 3f). Next, the simulated trajectories together with experimental camera noise and point spread function were used as input for microscopy simulations (Fig. 4c,d).

The simulated movies appear very similar to experimental ones (see Supplementary Video 1). Using the same analysis pipeline as that used for experimental data, we obtained statistics very similar to those of experimental movies (Fig. 5a and Supplementary Fig. 5b,c). Given this good agreement, we were confident in using the simulated movies to test the extent to which our analysis methods are able to reproduce the (known) underlying kinetic model, how much data is needed, and how robust the analysis is.

First, we analyzed simulated data, based on the default model (Fig. 4b) with the HMM analysis and AIC model selection as described above. The HMM successfully identified the four true diffusive states (Fig. 5b) as well as a fifth low-occupancy state with a very high diffusion constant, which we attribute to artifacts introduced by the tracking algorithms. Regarding the bound state, which is our primary interest, we saw that the HMM nicely extracts the correct mean dwell times and diffusion coefficients, whereas occupancy was underestimated, probably because the nucleoid excluded region is out of focus to a larger extent. Occupancies and diffusion coefficients for the faster states were reasonably well estimated, but the dwell times less so, possibly because of interference with the fast-spurious state.

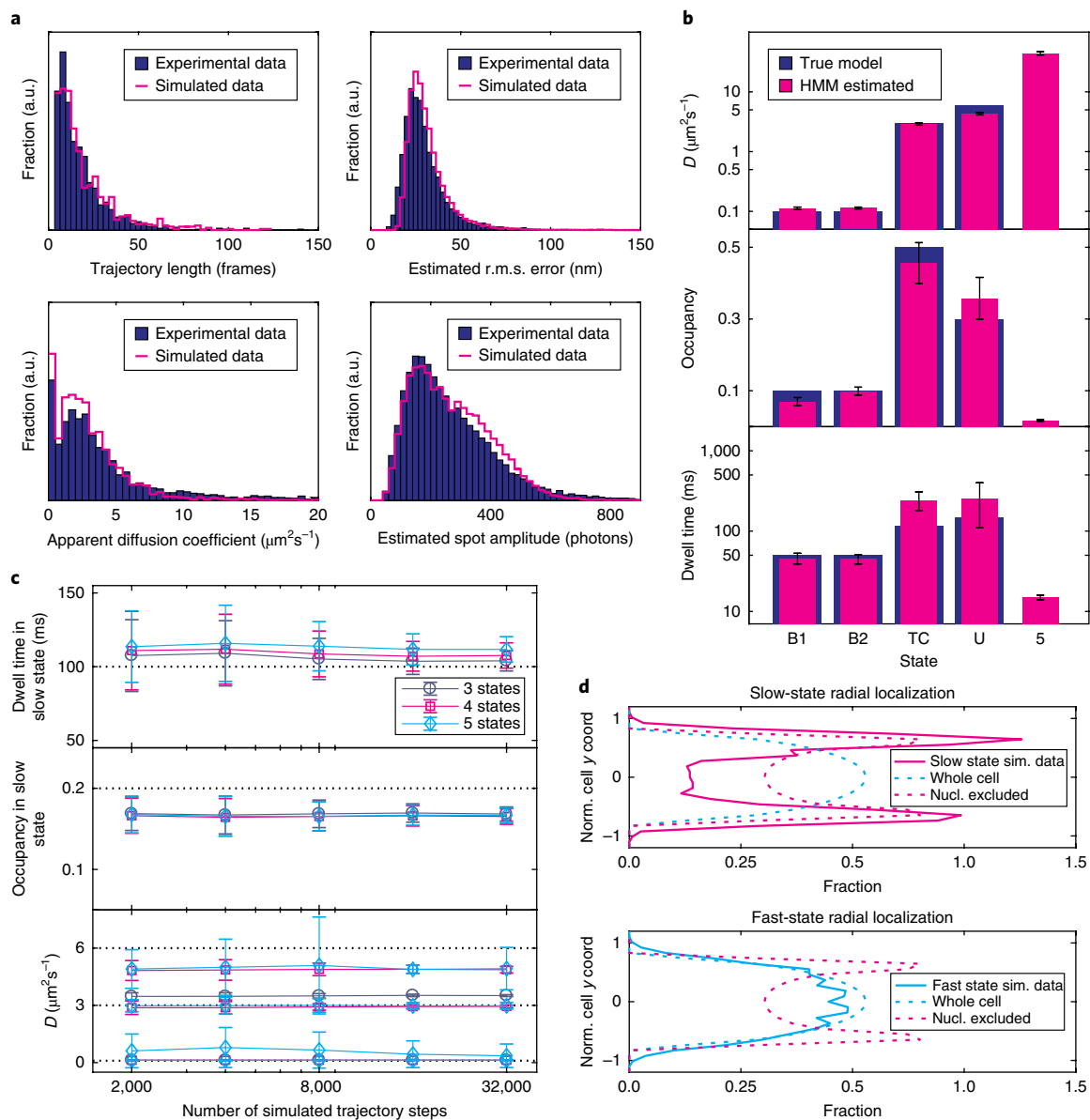


Fig. 5 | Analysis of simulated movies. **a**, Feature comparison of simulated ($n=16,389$) to experimental [Cy5]tRNA^{Phe} data (same as in Fig. 1e). **b**, Estimated HMM model parameters for the simulated data set. True values from the underlying kinetic model (Fig. 4b) are shown for comparison. **c**, Convergence of HMM-estimated diffusion constants and slow-state parameters. The graphs show mean and s.d. from >150 data sets resampled with replacements from a large data set of around 300,000 steps and analyzed with 3-, 4-, and 5-state HMMs. Dashed lines indicate true values (Fig. 4b). **d**, Radial distribution of slow ($<1\mu\text{m}^2/\text{s}$) and fast diffusive states, using the same data and HMM as in **a** and **b**. Spot locations were projected on the normalized short cell radial axis, as in the right panel of Fig. 2a. Dashed lines correspond to uniform distributions in the cytoplasm and nucleoid excluded regions. Error bars in the figure represent bootstrap estimates of standard error.

Second, we performed a convergence study without model selection to estimate the statistical uncertainty of the parameter estimates (Fig. 5c). Determining the bound-state mean dwell time with a standard error of 10 ms requires 8,000–16,000 diffusive steps. We also saw an upward bias of similar magnitude, probably due to the difficulty of detecting short events, and confirmed the bias in occupancy as well.

We next tested the robustness of our analysis to various perturbations. First, we found that our analysis successfully detects bound dwell times down to 50 ms but underestimates the mean dwell time by up to 25% when it exceeds the mean trajectory length (Supplementary Fig. 5d). Second, the estimated bound mean dwell time was influenced little by 50% changes in the intermediate diffusion constant D_{TC} (Supplementary Fig. 5e). However, though

the analysis detects the removal of the state (Supplementary Table 1, Sim. model 4), it yields a spurious increase in bound dwell time by about 50%. Third, we confirmed that camera calibration errors ($\pm 20\%$ EMCCD (electron multiplying charge-coupled device) gain error), which may affect the localization uncertainty estimates¹⁸, do not change bound state dwell times significantly (Supplementary Fig. 5f).

In light of these tests, we conclude that our combined single-particle tracking and HMM analysis is capable of extracting correct states, localization (Fig. 5d), and mean dwell times for diffusion constants up to about $3\mu\text{m}^2/\text{s}$ and 200 ms.

In vivo kinetics of translation initiation. Whereas translation elongation is a fairly simple and well-studied process, the dynamics

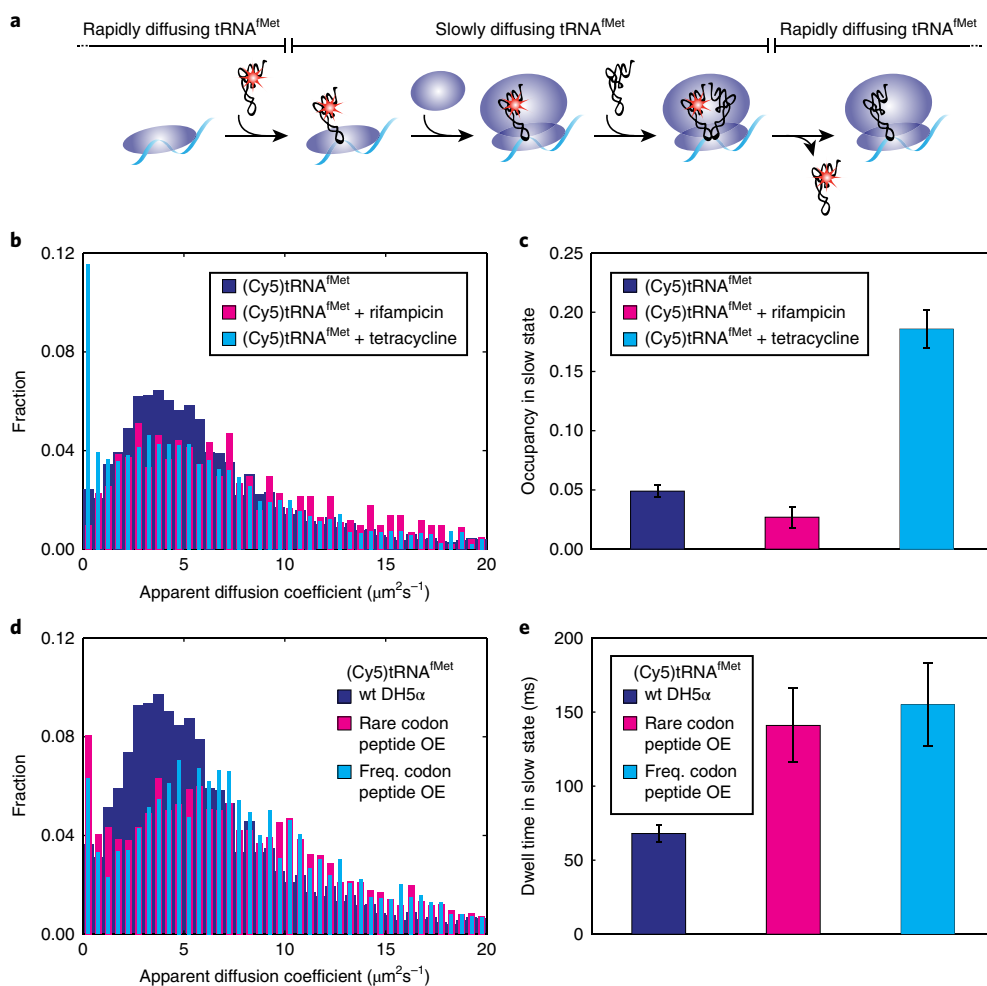


Fig. 6 | In vivo initiation kinetics using Cy5-labeled initiator tRNA^{fMet}. **a**, Simplified scheme displaying the predicted diffusional behavior of [Cy5]tRNA^{fMet} molecules being used on ribosomes. The dwell time of a functional [Cy5]tRNA^{fMet} binding event to a ribosome includes joining of the large ribosomal subunit and one cycle of peptide elongation. **b**, MSD-estimated apparent diffusion coefficients of [Cy5]tRNA^{fMet} in DH5α cells ($n = 31,498$) treated with rifampicin ($n = 8,389$) or tetracycline ($n = 21,259$). **c**, HMM estimated occupancy of [Cy5]tRNA^{fMet} in the slow diffusional state (see Supplementary Table 1). The trajectories used were the same as in **b**. **d**, MSD-estimated apparent diffusion coefficients of [Cy5]tRNA^{fMet} in DH5α cells overexpressing (OE) a short peptide with a rare Arg codon (AGG read by tRNA^{Arg4}; $n = 19,900$) or frequent Arg codon (CGU read by tRNA^{Arg2}; $n = 25,236$) in second position. **e**, HMM estimated dwell times for [Cy5]tRNA^{fMet} in the slow state with or without short peptides overexpressed (see Supplementary Table 1). The trajectories used were the same as in **d**. Error bars in **c** and **e** represent bootstrap estimates of standard errors.

of translation initiation is still poorly understood. In particular, to date, no conclusive results regarding the timing of translation initiation in *E. coli* is available, and estimates range from hundreds of milliseconds to hundreds of seconds per initiation event¹⁴. In vitro experiments using reconstituted systems suffer from the fact that the concentration of the individual components, such as the initiation factors, change the overall dynamics drastically; for example, the presence of initiation factor 3 slows down the 50S subunit joining step but at the same time makes the process more accurate^{15,16}. Hence, it is far from obvious under what conditions initiation of translation operates inside the cell. Furthermore, a long-standing question has been whether initiation limits the overall translation rate. A commonly held view has been that during nutrient-rich growth, translation elongation is fast because of high TC concentration and initiation is rate limiting³⁴.

To probe specifically the kinetics of translation initiation, we labeled *E. coli* tRNA^{fMet} with Cy5 and confirmed its activity in vitro (Supplementary Fig. 6a–c). In analogy to the [Cy5]tRNA^{Phe} experiments, the intention was to measure the time that [Cy5]tRNA^{fMet} spends bound to ribosomes, i.e., the time to dock the 50S subunit to

the fMet-tRNA^{fMet}·30S-mRNA pre-initiation complex and to finish the first elongation cycle (Fig. 6a).

We analyzed the diffusional behavior of fMet-[Cy5]tRNA^{fMet} in DH5α cells, and similarly to that seen with [Cy5]tRNA^{Phe}, we observed rapid diffusion of the [Cy5]tRNA^{fMet} interrupted by short dwells in a slow diffusion state (Supplementary Video 2). In contrast to [Cy5]tRNA^{Phe}, however, [Cy5]tRNA^{fMet} gives a very low fraction of molecules in the presumed ribosome-bound state (Fig. 6b,c), with HMM-estimated occupancy of merely 5% (Supplementary Table 1). Given that start codons are approximately ten times less frequent than Phe codons, this result might not seem so surprising, but this would also then require the tRNA^{fMet} dwell time on the ribosome to be considerably shorter than previous in vitro estimates of the time required to finish initiation. Indeed, HMM analysis results in a dwell time of 70 ms (± 10 ms) for [Cy5]tRNA^{fMet} in the slow state (Supplementary Table 1).

Provided that the first elongation cycle is as fast as an average cycle, i.e., around 50 ms, and that the probability of product formation once bound is close to one (in line with in vitro experiments^{15,35,36}), the estimated ribosome-bound dwell times of

[Cy5]tRNA^{fMet} thus suggest that the subunit joining step is completed within 20 ms. This result would imply that once fMet-tRNA^{fMet} has bound the small ribosomal subunit, initiation of translation is fast relative to an elongation cycle, and no build-up of pre-initiation or 70S ribosomes on start codons would be expected, contrary to what can be inferred from in vitro experiments¹⁴.

To confirm that the slow diffusion state of [Cy5]tRNA^{fMet} represents a ribosome-binding event, we investigated the effect of rifampicin and tetracycline also on [Cy5]tRNA^{fMet} diffusion. In presence of rifampicin, as with [Cy5]tRNA^{Phe}, the occupancy in the slow state decreases (3%, Fig. 6c). In the presence of tetracycline however, in contrast to the effect on [Cy5]tRNA^{Phe}, a significant increase of [Cy5]tRNA^{fMet} in the slow state (19%, Fig. 6c), with longer dwells (140 ± 40 ms), is seen (Supplementary Table 1). These results are in line with recent ribosome-profiling data²⁶ showing start-codon-specific stalling of ribosomes upon tetracycline treatment, suggesting authentic translation-dependent ribosome-binding events of [Cy5]tRNA^{fMet} in our assay.

Finally, to explore initiation of translation on a defined mRNA with potentially perturbed initiation kinetics, we electroporated fMet-[Cy5]tRNA^{fMet} into DH5 α cells overexpressing short peptides under the T7 promoter, including a rare or frequent Arg codon in second position, read by the low- and high-abundant tRNA^{Arg1} and tRNA^{Arg2} isoacceptors, respectively. We hypothesized that in the case of a rare Arg codon, depletion of the charged pool of the low-abundance tRNA would slow down ribosomes on the second codon with [Cy5]tRNA^{fMet} still bound to the ribosomal P site. We noted that induction severely inhibited cell growth in both cases (also confirmed in bulk experiment; see Supplementary Fig. 6d), suggesting that the protein synthesis machinery was to a large extent occupied by translation of the short mRNAs.

The diffusion pattern of [Cy5]tRNA^{fMet} changes significantly upon peptide overexpression (Fig. 6d). We find that the occupancy in the slow state increases slightly to 7% and 6% in the case of rare and frequent Arg codons, respectively (Supplementary Table 1), with a two-fold increase in dwell time for both cases compared to the wild-type strain (Fig. 6e). We see no increase in the slow-state occupancy or dwell time in cells expressing the T7 polymerase only (Supplementary Table 1). Overall, these results show that we can modulate the binding frequency and dwell time of fMet-[Cy5]tRNA^{fMet} by changing the transcriptome of the cells, further supporting authentic ribosome binding of the labeled tRNA. The fact that the slow-state dwell time increases to the same extent in both peptide-expressing strains, however, might indicate that the exhausted charged pool of neither of the tRNA isoacceptors is sufficient to support this high consumption level or possibly that some other component of the translational machinery gets limiting.

Discussion

In the present study, we have developed new experimental and analytical approaches to directly measure reaction rates inside living cells using electroporated fluorescent molecules. By using small organic dyes, we overcome the limitations of fluorescent proteins and are able to target biological processes with minimal disturbances and follow individual molecules in reaction cycles for extensive periods of time. Similarly to the work recently published by Plochowitz et al.⁵, we make use of established protocols for in vitro dye-labeling of tRNAs^{12,37}. However, whereas Plochowitz et al.⁵ electroporated bulk tRNA and never approached kinetics, we use specific tRNA species and can hence extract codon-specific tRNA dwell times on ribosomes with our new analytical tools.

By electroporation and tracking of Cy5-labeled tRNA molecules, we directly measure translation kinetics in exponentially growing *E. coli* cells. Trajectories are fitted using machine-learning algorithms, and we estimate the mean dwell time and occupancy of the tRNAs in different diffusional states. The absolute number of distinct

diffusional states is difficult to estimate. AIC is known to sometimes overfit HMM-like models³⁸, but the large number of states could also reflect experimental artifacts such as tracking errors or the complexity that goes beyond the model assumptions, for example, in-sample variability from cell-to-cell variability, micro-heterogeneity in the cytoplasm³⁹, or variability in bound-state properties when ribosomes bind to mRNAs of different sizes or occupancy (polysomes). We also find systematic differences in diffusive states in different bacterial strains (compare, for example, [Cy5]tRNA^{Phe} data in DH5 α and MG1655) or in different growth conditions. This might reflect differences in cytoplasm composition because of altered growth rates or treatment with antibiotics (as has been observed previously²⁰), or variability in tracking artifacts due to cell geometry variations. Judging from analyses of simulated microscopy data, we also see that faster diffusive species are significantly harder to track than slower ones with the current exposure timings (Fig. 5b). Thus, it is possible that the HMM/AIC analysis finds extra states in addition to those reflecting the biochemical reaction cycle. To circumvent these difficulties, and because our main interest here is ribosome-binding events of tRNAs, we coarse-grained the AIC-optimal models with many states to two-state models, representing ribosome-bound or unbound tRNA species. The choice of threshold, $1 \mu\text{m}^2/\text{s}$, was based on previous single-particle tracking data of ribosomal subunits^{1,20,25}, but increasing or decreasing the threshold by $0.5 \mu\text{m}^2/\text{s}$ only changes some of the numbers slightly (Supplementary Table 1) and does not affect the conclusions of this study. Similarly, our conclusions are insensitive to the exact number of states in detailed models.

We find the mean dwell time of tRNA^{Phe} in the slowly diffusing, ribosome-bound state, about 100 ms, to be in good agreement with previous measurements of average elongation rates in vivo, i.e., 50 ms per codon²⁸. Similar to the bulk tRNA tracking shown in Plochowitz et al.⁵, we also find binding events of tRNA^{Phe} to ribosomes mainly in the periphery of the cells, in accordance with nucleoid excluded translation^{1,20}, and our tentatively assigned free tRNA diffusional state ($6.5 \mu\text{m}^2/\text{s}$, Supplementary Table 1) agrees fairly well with their finding ($8 \mu\text{m}^2/\text{s}$).

A direct comparison to in vitro results is complicated, because the 100 ms average dwell time includes the binding of an average ternary complex to the A site, and we know from previous analyses that there is a big variation in peptide bond formation rates dependent on aa-tRNA identity⁴⁰. However, assuming $k_{\text{cat}} = 130 \text{ s}^{-1}$ for peptide bond formation for all aa-tRNAs⁷, $k_{\text{cat}}/K_m = 80 \mu\text{M}^{-1}\text{s}^{-1}$ for the same process for an average ternary complex binding to the A site (in accordance with the Mg²⁺ titrations in⁴¹ and the in vitro-in vivo calibration in⁴²), and, on average, $2 \mu\text{M}$ available cognate ternary complex in the cell^{43,44}, we can subtract peptide bond formation times and are left with 40 ms per elongation factor G (EF-G) catalyzed translocation step, which is in good agreement with results from in vitro experiments performed under in vivo like conditions^{29,42}.

Moving on to unknown territory, we find the mean dwell time of initiator fMet-tRNA^{fMet} on ribosomes to be surprisingly short, around 70 ms (with an uncertainty of about 20% judging from the analysis of simulated data), which is on the lower limit of what has been reported from reconstituted systems^{16,35}. These results suggest that initiation of translation is fast once the 30S-fMet-tRNA^{fMet} pre-initiation complex has formed and that these steps do not represent a bottle neck during translation, as can be inferred from in vitro kinetics experiments^{14,16,29,44}.

In conclusion, we have developed new experimental and analytical tools for direct measurement of reaction kinetics in live cells, using fluorescently labeled tRNAs as a case study. We have quantitatively validated our analysis through extensive analyses of microscopy simulations, which include a cell-like geometry and experimentally derived background fluorescence, camera noise, and optical point-spread function. We are optimistic that this

combination of experimental methods, data analysis, and careful validation on simulated microscopy data will open up new possibilities to calibrate the wealth of knowledge obtained from *in vitro* biochemistry to the conditions in living cells and to further explore the dynamics of biochemical pathways *in vivo*, including but not limited to the protein synthesis machinery.

Methods

Methods, including statements of data availability and any associated accession codes and references, are available at <https://doi.org/10.1038/s41589-018-0063-y>.

Received: 13 September 2017; Accepted: 9 April 2018;

Published online: 16 May 2018

References

- Sanamrad, A. et al. Single-particle tracking reveals that free ribosomal subunits are not excluded from the *Escherichia coli* nucleoid. *Proc. Natl. Acad. Sci. USA* **111**, 11413–11418 (2014).
- Uphoff, S., Reyes-Lamothe, R., Garza de Leon, F., Sherratt, D. J. & Kapanidis, A. N. Single-molecule DNA repair in live bacteria. *Proc. Natl. Acad. Sci. USA* **110**, 8063–8068 (2013).
- Persson, F., Lindén, M., Unoson, C. & Elf, J. Extracting intracellular diffusive states and transition rates from single-molecule tracking data. *Nat. Methods* **10**, 265–269 (2013).
- Crawford, R. et al. Long-lived intracellular single-molecule fluorescence using electroporated molecules. *Biophys. J.* **105**, 2439–2450 (2013).
- Plochowitz, A., Farrell, I., Smilansky, Z., Cooperman, B. S. & Kapanidis, A. N. *In vivo* single-RNA tracking shows that most tRNA diffuses freely in live bacteria. *Nucleic Acids Res.* **45**, 926–937 (2017).
- Cochella, L. & Green, R. An active role for tRNA in decoding beyond codon:anticodon pairing. *Science* **308**, 1178–1180 (2005).
- Johansson, M., Bouakaz, E., Lovmar, M. & Ehrenberg, M. The kinetics of ribosomal peptidyl transfer revisited. *Mol. Cell* **30**, 589–598 (2008).
- Sievers, A., Beringer, M., Rodnina, M. V. & Wolfenden, R. The ribosome as an entropy trap. *Proc. Natl. Acad. Sci. USA* **101**, 7897–7901 (2004).
- Selmer, M. et al. Structure of the 70S ribosome complexed with mRNA and tRNA. *Science* **313**, 1935–1942 (2006).
- Valle, M. et al. Incorporation of aminoacyl-tRNA into the ribosome as seen by cryo-electron microscopy. *Nat. Struct. Biol.* **10**, 899–906 (2003).
- Demeshkina, N., Jenner, L., Westhof, E., Yusupov, M. & Yusupova, G. A new understanding of the decoding principle on the ribosome. *Nature* **484**, 256–259 (2012).
- Blanchard, S. C., Kim, H. D., Gonzalez, R. L. Jr., Puglisi, J. D. & Chu, S. tRNA dynamics on the ribosome during translation. *Proc. Natl. Acad. Sci. USA* **101**, 12893–12898 (2004).
- Chen, J. et al. Dynamic pathways of -1 translational frameshifting. *Nature* **512**, 328–332 (2014).
- Rodnina, M. V. The ribosome in action: Tuning of translational efficiency and protein folding. *Protein Sci.* **25**, 1390–1406 (2016).
- Antoun, A., Pavlov, M. Y., Lovmar, M. & Ehrenberg, M. How initiation factors maximize the accuracy of tRNA selection in initiation of bacterial protein synthesis. *Mol. Cell* **23**, 183–193 (2006).
- Antoun, A., Pavlov, M. Y., Lovmar, M. & Ehrenberg, M. How initiation factors tune the rate of initiation of protein synthesis in bacteria. *EMBO J.* **25**, 2539–2550 (2006).
- Loy, G. & Zelinsky, A. Fast radial symmetry for detecting points of interest. *IEEE Trans. Pattern Anal. Mach. Intell.* **25**, 959–973 (2003).
- Lindén, M., Čurić, V., Amselem, E. & Elf, J. Pointwise error estimates in localization microscopy. *Nat. Commun.* **8**, 15115 (2017).
- Jaqaman, K. et al. Robust single-particle tracking in live-cell time-lapse sequences. *Nat. Methods* **5**, 695–702 (2008).
- Bakshi, S., Siryaporn, A., Goulian, M. & Weisshaar, J. C. Superresolution imaging of ribosomes and RNA polymerase in live *Escherichia coli* cells. *Mol. Microbiol.* **85**, 21–38 (2012).
- Burnham, K. P. & Anderson, D. R. *Model Selection and Multimodel Inference: a Practical Information-theoretic Approach*. 2nd edn. (Springer, New York, 2002).
- Furano, A. V. Content of elongation factor Tu in *Escherichia coli*. *Proc. Natl. Acad. Sci. USA* **72**, 4780–4784 (1975).
- Avcilar-Kucukgoze, I. et al. Discharging tRNAs: a tug of war between translation and detoxification in *Escherichia coli*. *Nucleic Acids Res.* **44**, 8324–8334 (2016).
- Dittmar, K. A., Sørensen, M. A., Elf, J., Ehrenberg, M. & Pan, T. Selective charging of tRNA isoacceptors induced by amino-acid starvation. *EMBO Rep.* **6**, 151–157 (2005).
- Balzarotti, F. et al. Nanometer resolution imaging and tracking of fluorescent molecules with minimal photon fluxes. *Science* **355**, 606–612 (2017).
- Nakahigashi, K. et al. Comprehensive identification of translation start sites by tetracycline-inhibited ribosome profiling. *DNA Res.* **23**, 193–201 (2016).
- Chen, J., Petrov, A., Tsai, A., O’Leary, S. E. & Puglisi, J. D. Coordinated conformational and compositional dynamics drive ribosome translocation. *Nat. Struct. Mol. Biol.* **20**, 718–727 (2013).
- Liang, S. T., Xu, Y. C., Dennis, P. & Bremer, H. mRNA composition and control of bacterial gene expression. *J. Bacteriol.* **182**, 3037–3044 (2000).
- Borg, A. & Ehrenberg, M. Determinants of the rate of mRNA translocation in bacterial protein synthesis. *J. Mol. Biol.* **427**, 1835–1847 (2015).
- Bilgin, N., Claessens, F., Pahverk, H. & Ehrenberg, M. Kinetic properties of *Escherichia coli* ribosomes with altered forms of S12. *J. Mol. Biol.* **224**, 1011–1027 (1992).
- Ruusalta, T., Andersson, D., Ehrenberg, M. & Kurland, C. G. Hyper-accurate ribosomes inhibit growth. *EMBO J.* **3**, 2575–2580 (1984).
- Fange, D., Mahmutovic, A. & Elf, J. MesoRD 1.0: Stochastic reaction-diffusion simulations in the microscopic limit. *Bioinformatics* **28**, 3155–3157 (2012).
- Lindén, M., Čurić, V., Boucharin, A., Fange, D. & Elf, J. Simulated single molecule microscopy with SMEagol. *Bioinformatics* **32**, 2394–2395 (2016).
- Subramaniam, A. R., Zid, B. M. & O’Shea, E. K. An integrated approach reveals regulatory controls on bacterial translation elongation. *Cell* **159**, 1200–1211 (2014).
- Goyal, A., Belardinelli, R., Maracci, C., Milón, P. & Rodnina, M. V. Directional transition from initiation to elongation in bacterial translation. *Nucleic Acids Res.* **43**, 10700–10712 (2015).
- Milon, P. et al. The ribosome-bound initiation factor 2 recruits initiator tRNA to the 30S initiation complex. *EMBO Rep.* **11**, 312–316 (2010).
- Pan, D., Qin, H. & Cooperman, B. S. Synthesis and functional activity of tRNAs labeled with fluorescent hydrazides in the D-loop. *RNA* **15**, 346–354 (2009).
- Smith, A., Naik, P. A. & Tsai, C. L. Markov-switching model selection using Kullback-Leibler divergence. *J. Econom.* **134**, 553–577 (2006).
- Mondal, J., Bratton, B. P., Li, Y., Yethiraj, A. & Weisshaar, J. C. Entropy-based mechanism of ribosome-nucleoid segregation in *E. coli* cells. *Biophys. J.* **100**, 2605–2613 (2011).
- Johansson, M. et al. pH-sensitivity of the ribosomal peptidyl transfer reaction dependent on the identity of the A-site aminoacyl-tRNA. *Proc. Natl. Acad. Sci. USA* **108**, 79–84 (2011).
- Zhang, J., Jeong, K. W., Johansson, M. & Ehrenberg, M. Accuracy of initial codon selection by aminoacyl-tRNAs on the mRNA-programmed bacterial ribosome. *Proc. Natl. Acad. Sci. USA* **112**, 9602–9607 (2015).
- Zhang, J., Jeong, K. W., Mellenius, H. & Ehrenberg, M. Proofreading neutralizes potential error hotspots in genetic code translation by transfer RNAs. *RNA* **22**, 896–904 (2016).
- Dong, H., Nilsson, L. & Kurland, C. G. Co-variation of tRNA abundance and codon usage in *Escherichia coli* at different growth rates. *J. Mol. Biol.* **260**, 649–663 (1996).
- Gromadski, K. B., Daviter, T. & Rodnina, M. V. A uniform response to mismatches in codon-anticodon complexes ensures ribosomal fidelity. *Mol. Cell* **21**, 369–377 (2006).

Acknowledgements

We thank S. Sanyal and M. Ehrenberg (Uppsala University) for sharing components of the reconstituted protein synthesis system; D. Hughes (Uppsala University) for the CH2273 strain; P. Leroy (Uppsala University) for construction of the PL22A9 EF-Tu-mEos2 strain; P. Walter (UCSF) for the pDMF6 plasmid; K. Kipper, A. Boucharin, V. Čurić and D. Fange for providing technical expertise; E. Amselem for measuring the PSE, and M. Ehrenberg and J. Puglisi for comments on the manuscript. This work was supported by The Swedish Research Council (2015-04111, M.J.), The Wenner-Gren Foundations (M.J., I.L.V.), Carl Tryggers Stiftelse för Vetenskaplig Forskning (CTS 15:243, M.J.), the European Research Council (ERC-2013-CoG 616047 SMILE, J.E.), and Knut and Alice Wallenberg Foundation (J.E.).

Author contributions

M.J. conceived the project, except for the data analysis and simulation pipelines, which were conceived by M.L. and J.E. M.J. and I.L.V. designed experiments. I.L.V. performed and analyzed *in vivo* experiments. M.L. generated and analyzed simulated data and wrote analysis code. J.A.R. and M.M. participated in method development and provided reagents. K.-W.I. performed *in vitro* experiments. M.J., M.L., J.E. and I.L.V. wrote the manuscript.

Competing interests

The authors declare no competing interest.

Additional information

Supplementary information is available for this paper at <https://doi.org/10.1038/s41589-018-0063-y>.

Reprints and permissions information is available at www.nature.com/reprints.

Correspondence and requests for materials should be addressed to M.J.

Publisher’s note: Springer Nature remains neutral with regard to jurisdictional claims in published maps and institutional affiliations.

Methods

Experimental details. tRNA labeling and charging. For coupling of Cy5 to the 4-thiouridine at position 8 of *E. coli* tRNA^{Met} (Chemical Block, Russia) 16 nmol of tRNA^{Met} in 75 μ l of labeling buffer (50 mM Tris-HCl, pH 8.5) was added to 1 vial of dry disulfo-Cy5 mono-reactive maleimide dye (GE Healthcare) and incubated at 37 °C with occasional vortexing. After 3 h, the labeling mixture was transferred to a new vial of the same dye and incubated for 3 more hours. Then 0.1 volume of 3 M NaOAc (pH 5.0) was added, and unreacted dye was removed by phenol-chloroform extraction (phenol:chloroform 5:1 v/v, pH 4.5). The tRNA was then precipitated in EtOH and finally dissolved in Milli-Q water. Typical labeling yield was $10 \pm 3\%$.

For coupling of Cy5 to the 3-(3-amino-3-carboxypropyl)uridine at position 47 of *E. coli* tRNA^{Phe} (tRNA Probes), 12 nmol of tRNA^{Phe} in 85 μ l of labeling buffer (0.9 M NaCl, 50 mM Na-HEPES, pH 8.0) was mixed with 1 μ l of 320 mM disulfo-Cy5 mono-reactive NHS ester dye (Lumiprobe) dissolved in anhydrous DMSO and incubated at 30 °C with occasional vortexing. After 6 h, with another 1 μ l of dye added after 3 h, 0.1 volume of 3 M NaOAc (pH 5.0) was added, and unreacted dye was removed as described for tRNA^{Met}. Typical labeling yield was approximately 70%.

3'-terminus labeling of tRNA^{Phe}. First, for 3' ribose oxidation, tRNA^{Phe} (59 μ M final) was mixed with NaOAc (100 mM final, pH 5.0) and freshly dissolved KIO₄ (5 mM final) in 60 μ l and incubated on ice for 35 min. To quench the reaction 7 μ l of 100 mM ethylene glycol was added and allowed to react for an additional 5 min on ice. The tRNA was precipitated twice in EtOH and redissolved in 25 μ l of labeling buffer (100 mM NaOAc pH 5.0 and 200 mM KCl). The sample was mixed with 0.3 μ l of 75 mM disulfo-Cy5 mono-reactive hydrazide dye (Cyandyes) dissolved in anhydrous DMSO and incubated at room temperature (21–23 °C) with occasional vortexing. After 5 h, with another 0.3 μ l dye added after 2.5 h, unreacted dye was removed as described for tRNA^{Met}. Typical labeling yield was $24 \pm 4\%$.

[Cy5]-3'-tRNA^{Phe} was purified from unlabeled tRNA using RP-HPLC. The tRNA was eluted at room temperature and a flow rate of 0.5 ml/min applying a linear gradient of 15–90% buffer B in buffer A over 58 min (buffer A: 20 mM NH₄OAc, 10 mM MgCl₂, 400 mM NaCl, pH 5.0 in water; buffer B: 20 mM NH₄OAc, 10 mM MgCl₂, 400 mM NaCl, pH 5.0 in 80% (v/v) MeOH in water). Collected fractions were concentrated using 3 kDa spin column (Millipore). From absorbance of the final sample, the fluorophore-to-tRNA ratio for [Cy5]-3'-tRNA^{Phe} was determined as 0.95.

Aminoacylation of [Cy5]tRNA^{Phe} was performed by incubating [Cy5]tRNA^{Phe} (12 nmol in 500 μ l final) at 37 °C for 30 min in buffer (50 mM Tris-HCl, pH 7.5, 50 mM KCl, 10 mM MgCl₂) supplemented with ATP (1 mM), PEP (10 mM), β -mercaptoethanol (3 mM), PPase (10 μ g/ml), PK (50 μ g/ml), MK (2 μ g/ml), Phe (200 μ M), and PheRS (0.6 μ M). The reaction was quenched by the addition of 0.1 volume of 3 M NaOAc (pH 5.0) and enzymes were removed by phenol-chloroform extraction (phenol:chloroform 5:1 v/v, pH 4.5). Phe-[Cy5]tRNA^{Phe} was purified from unlabeled and deacylated tRNAs using RP-HPLC (Fig. 1a) as described above for [Cy5]-3'-tRNA^{Phe} with resulting fluorophore-to-tRNA ratio equal to 1.

[Cy5]tRNA^{Met} was purified after labeling using RP-HPLC (Supplementary Fig. 6) as described above, but with the linear gradient of 25–90% buffer B in A over 50 min, with the resulting fluorophore-to-tRNA ratio equal to 0.9. Aminoacylation and formylation of [Cy5]tRNA^{Met} (1,200 pmol in 500 μ l final) was performed in the same way as aminoacylation of [Cy5]tRNA^{Phe}, with the following changes: Met (200 μ M) and MetRS (1 U/ μ l) instead of Phe and PheRS, and the addition of methionyl-tRNA formyltransferase (2 U/ μ l) and 10-formyltetrahydrofolate (1 mM). fMet-[Cy5]tRNA^{Met} were finally purified from deacylated (and nonformylated) tRNAs using RP-HPLC as described above for [Cy5]-3'-tRNA^{Phe} (Supplementary Fig. 6).

Purified tRNAs samples were stored in frozen aliquots (–80 °C) at 9–12 μ M concentration in 5 mM KOAc, 10 mM KCl, and 0.2 mM MgOAc (pH 6.1) (buffer exchanged using Bio-Spin P-6 gel filtration columns). [Cy5]-3'-tRNA^{Phe} was stored at a 3 μ M concentration in Milli-Q water.

Cell strains and media. ElectroMAX DH5 α -E electrocompetent cells (Invitrogen), referred to as DH5 α in the main text, were diluted five times with 10% glycerol water solution and stored in 20 μ l aliquots at –80 °C.

The CH2273 strain (a kind gift from D. Hughes), with SmP (streptomycin pseudodependent) phenotype is a reconstructed version of CH184 (ref. 45) and carries two mutations (P91Q and R86S) in ribosomal protein S12 (*rpsL*) in an MG1655 background.

The EF-Tu-mEos2 fusion (in strain PL22A9) was created by lambda-red recombination in strain BW25993 of a PCR fragment containing mEos2-CmR downstream of *tufA*. Homology to the 3' region of *tufA* was included in the PCR primers, *tufA*-mEos2_Fw and *tufA*_3'_P1_CmR_Rev (sequences below). As template, an existing in-lab plasmid containing mEos2 linked to a CmR cassette was used.

For observation of translation initiation on a defined mRNA, a T7-polymerase driven expression system was established in the DH5 α strain as follows. DH5 α cells were transformed with pCS6 (Addgene plasmid #55752)⁴⁶ bearing the T7 polymerase gene and pET3c-MRLFV bearing a short peptide sequence shown to

be nontoxic to the cell⁴⁷ under T7 polymerase promoter. Two variants with rare (AGG) and frequent (CGU) arginine codons were prepared. pET3c-MR⁴⁸LfV and pET3c-MR⁴⁹LfV were made by PCR amplification of the whole pDMF6 backbone (pET3c derivative) using the reverse primer longPCR_RV containing an NdeI restriction site and the forward longPCR_ArgR_FW or longPCR_ArgF_FW primers, respectively (see sequences below) containing both the peptide gene and an NdeI restriction site in an overhang. The linear PCR product was digested with NdeI and then self-ligated. In order to check to what extent expression of T7 polymerase affects cells, DH5 α cells carrying only the pCS6 plasmid were used.

Cells (except unmodified DH5 α) were prepared as electrocompetent based on the procedure suggested in ref. 48. A low-density LB overnight culture ($OD_{600} \leq 0.5$) was diluted 100–200 times in SOB medium (lacking Mg²⁺). Cells were grown at 37 °C until they reached $OD_{600} = 0.4$, then cooled in an ice-water bath for 30 min, harvested and washed four times with cold 10% glycerol water solution. The OD_{600} was adjusted to 60 ± 10 , and cells were aliquoted (20 μ l) and frozen in an EtOH/dry ice bath for storage or used immediately without freezing.

In bulk, the CH2273 strain was grown in the presence of streptomycin 100 μ g/ml, and cells with plasmids were grown in the presence of antibiotics corresponding to existing antibiotic resistance cassettes (spectinomycin, 30 μ g/ml for pCS6, and carbenicillin, 100 μ g/ml for pET3c-MRLFV). Antibiotics were omitted from the cell washing step and in later steps, including recovery after electroporation and microscopy experiments.

EZ Rich Defined Medium (RDM, from Teknova) with glucose (0.2%) as carbon source was reconstituted, aliquoted, and stored frozen at –20 °C. SOB medium, lacking Mg²⁺ (2.0% tryptone, 0.5% yeast extract, 10 mM NaCl, 2.5 mM KCl, pH 7.0) was prepared in house.

Primers for plasmid construction and lambda-red recombination. longPCR_RV: 5'-GATCGGTTAAATTATCAAACATATGTATATCTCC-3'

longPCR_ArgR_FW: 5'-TCATATCATATGAGGTTATTTGTTTAAAGGATCCGGCTGCTAACAAAG-3' (Arg codon is underlined)

longPCR_ArgF_FW: 5'-TCATATCATATGCGTTTATTTGTTTAAAGGATCCGGCTGCTAACAAAG-3' (Arg codon is underlined)

tufA-mEos2_Fw: 5'-CGTACCCTGGCGCGGGCGTTGTTGCTAAAG-TTCTGGGCATGAGTGCATTAAGCCAGAC-3' (Homology to 3' of *tufA* is underlined)

*tufA*_3'_P1_CmR_Rev: 5'-CGTTCTGACAGTACGAATAAGATATGCCGTCAACAAATGCCAAGCAGCTCCAGCTACAC-3' (Homology to downstream region of *tufA* is underlined)

In vitro dipeptide assay. Rapid kinetics dipeptide experiments using dye-labeled or unlabeled tRNAs were performed in polymix buffer in a quench-flow instrument according to ref. 7. For [Cy5]tRNA^{Phe} experiments, 70S initiation complex carrying f[³H]Met-tRNA^{Met} in P site and displaying UUU codon in A site were reacted with the preformed Phe-[Cy5]tRNA^{Phe}-EF-Tu-GTP (or unlabeled Phe-tRNA^{Phe}) ternary complex. For [Cy5]tRNA^{Met} experiments, 70S initiation complex carrying fMet-[Cy5]tRNA^{Met} in P site (or unlabeled fMet-tRNA^{Met}) and displaying UUU codon in A site were reacted with the preformed [³H]Phe-tRNA^{Phe}-EF-Tu-GTP ternary complex. The extent of dipeptide formed was analyzed using RP-HPLC, and the data were fitted to a single-exponential equation using Origin (OriginLab). All components of the reconstituted protein synthesis system were a kind gift from Ehrenberg and Sanyal labs (Uppsala University, Sweden). The purification procedures of the components have been published in detail before (for example, ref. 7 and references therein).

Cell growth rates in bulk. Cells were grown overnight at 37 °C in RDM. 0.4–0.5 μ l of overnight culture (the volume was adjusted to have equal final optical densities for different cell strains) were then inoculated in 200 μ l fresh preheated RDM on a microplate, and cells were grown at 37 °C in a microplate reader (Infinite M200 or Spark 10M, Tecan). Optical densities were measured every 5 min with a prior 1 min orbital shaking.

For the CH2273 strain, the overnight culture was grown in the presence of streptomycin (100 μ g/ml) and diluted on the plate in the fresh RDM with or without streptomycin (100 μ g/ml).

For overexpression of short peptides, modified DH5 α cells and DH5 α (with pCS6 only) were grown according to the general description above up to early exponential phase when expression of the peptide was induced by addition of arabinose (0.2%) and cAMP (1 mM). For non-induced cells, an equivalent volume of RDM was added.

A blank was subtracted from the growth curves, and the exponential part of the curve was fitted with a rise exponential function in MagicPlot (MagicPlot Systems). For presentation in Supplementary Figs. 4 and 6, the data from one experiment (4–5 individual wells) were averaged. For doubling time estimation, the data from two independent experiments (4–5 individual wells each) were fitted separately and the results were averaged.

Electroporation and microscopy. 20 μ l of cells ($OD_{600} = 60 \pm 10$) were mixed with 2 pmol dye-labeled tRNA and incubated on ice for 1 min. The sample was transferred

into an ice-cold 1 mm electroporation cuvette. Electroporation was performed using a MicroPulser instrument (Bio-Rad) by applying a 1.9 kV pulse (1.5 kV for MG1655 and CH2273 strains), which typically resulted in a decay time constant of 5.7 ± 0.1 ms. 500 μ l of RDM (room temperature) was immediately added to the cuvette, and the cells were allowed to recover for 30 min with shaking at 37 °C. The cells were then harvested by centrifugation (1,150 rcf, 75 s) and washed three times with 37 °C RDM medium to remove non-internalized tRNA. Cells were resuspended in RDM to $OD_{600} = 0.03$ and sparsely spread onto a 2% agarose pad (made with RDM) containing 3 μ M of SYTOX Blue dead-cell stain. The sample was mounted on the microscope, where single cells were allowed to grow and divide to form mini-colonies of the size of 4–8 cells before imaging. The temperature of the sample was maintained at 37 ± 2 °C using a cage incubator encapsulating the microscope stage.

For rifampicin (200 μ g/ml) and tetracycline (10 μ g/ml) treatment, RDM containing antibiotic and SYTOX blue (3 μ M) was injected to the sample with mini-colonies approximately 100 min after sample preparation. Imaging was performed 70–200 min later.

For overexpression of the short peptide, cells were allowed to form mini colonies, and injection of RDM containing arabinose (0.2%), cAMP (1 mM) and SYTOX blue (3 μ M) was performed approximately 70 min after sample preparation. Imaging was performed 80–180 min later. In the control experiment with cells carrying only the pCS6 plasmid, induction was made by the injection of the same medium approximately 40 min after sample preparation, and imaging was performed 70–140 min later.

For tracking of the EF-Tu-mEos2 fusion protein, an overnight culture of the PL22A9 strain in LB was diluted in RDM and grown until $OD_{600} \approx 0.7$. Cells were then spread onto a 2% agarose RDM pad and grown for about 1 h at 37 °C before data acquisition.

Each microscopy experiment was performed in 2–5 replicas (each comprising 10–100 cell colonies with internalized [Cy5]tRNA. See Supplementary Table 1 for number of replicas) on different dates, generally using the same batches of electrocompetent cells and labeled tRNAs. The data was found to be consistent in between different repetitions and were combined for analysis.

Optical setup. An inverted microscope (Nikon Ti-E) with a CFI Apo TIRF 100 \times 1.49 NA (Nikon) objective was used. Fluorescence and bright-field images were recorded on an Andor iXon 897 Ultra EMCCD camera equipped with an additional 2.0 \times lens (Diagnostic Instruments DD20NLT). For phase contrast imaging, an Infinity 2-5M (Lumenera) camera was used. For [Cy5]tRNA tracking, a 639 nm laser (Coherent Genesis MX 639-1000 STM) with a power density of 4.5 kW/cm² on the sample plane was used in stroboscopic illumination mode with 1.5 ms laser/5 ms camera exposures. For SYTOX Blue imaging, a 405 nm laser (Cobolt MLD) with a power density of 17 W/cm² on the sample plane was used with continuous exposure of 21 ms.

For EF-Tu-mEos2 fusion protein tracking, cells were pre-bleached with 561 nm laser (Coherent Genesis MX 561-500 STM) (2 kW/cm², 5 s continuous exposure) in order to reduce fluorescent background. Then the photoswitchable mEos2 protein was activated with 405 nm laser (17 W/cm², 2 s continuous exposure), and tracking was performed with the same 561 nm laser in stroboscopic illumination mode with 4 ms laser/5 ms camera exposures.

The microscope was controlled using μ Manager, and automated acquisitions were performed using an in-house written μ Manager plugin.

Simulated single-molecule microscopy. *Simulated reaction-diffusion kinetics.* The simulation geometry is illustrated in Fig. 4a, and the simulation parameters of the simulated models are given in Supplementary Table 2, where model 1 corresponds to the default model. The corresponding MesoRD model files are included in the open research repository Zenodo at <https://zenodo.org/record/1168228#>. WuG1i5uaUk.

PSF measurement. As a model of point-sources, fluorescent microspheres (FluoSpheres F8783) of size 0.02 μ m were excited by 639 nm laser and imaged with the objective described above and a DMK 23U274 camera (The Imaging Source). The resulting image pixel size was 44 nm. A z-stack with 50 nm steps over a range of 10 μ m was acquired with 300 ms exposure time.

PSF model construction. (Supplementary Fig. 5a). A 100-by-100 pixel area with a single spot was manually selected, and a range of 61 image z-steps was extracted. The raw data was de-noised by removing an offset/background threshold of 1,000 (roughly the 80% intensity quantile) and applying a mask, constructed as follows. First, pixels with intensity above the threshold were set to 1, and zero otherwise. Second, a morphological opening operation was applied (an erosion followed by a dilation) using a structuring element in the form of disk of radius 2 pixels, to remove small islands of spurious intensity, and finally normalize each image plane by the total intensity of the brightest plane. The reference position (x_0, y_0) of the PSF model was taken to be the radial symmetry center⁴⁹ at the focal plane.

PSF simulation. During SMeagol⁵³ simulations, a simulated photon emission event at (x_E, y_E, z_E) generates a photon on the camera chip at position $(x_E + \Delta x, y_E + \Delta y)$.

We define the 2-dimension distribution of $(\Delta x, \Delta y)$ relative to the reference position $(x_0, y_0) = (x_E, y_E)$ to be proportional to the normalized pixel intensity of the above PSF model, uniformly distributed in the PSF model pixels. Note that the normalized intensity, which we call $p_f(z)$, is less than 1 for all image planes but one. We take this to mean that there is a finite probability $1 - p_f(z)$ that the emitted photon is scattered outside the camera chip, which effectively models a z-dependent spot intensity. For efficient sampling, we factorize the PSF distribution as $p(\Delta x, \Delta y | z) = p_f(\Delta x, \Delta y < \infty | z) p_x(\Delta x | z) p_y(\Delta y | \Delta x, z)$, and create z-dependent lookup tables for p_f , p_x , and p_y which are used during simulation. Matlab functions for constructing and sampling from the PSF model is attached in the Supplementary Software.

Simulated video microscopy. The simulated movies are built in steps, starting from an experimental background and then looping through each simulated cell position, where a few new fluorophore traces are added on top of the output from the previous iteration. A set of a few experimental background movies was used, in which intensities varied slightly within experimental reproducibility. Because the simulation software does not generate phase contrast images, we simulated well-separated cells and did not try to simulate the cell segmentation process. An example script of this simulation protocol, including runinput files and an experimental background movie, is given in the supplementary software.

Quantification and statistical analysis. *Camera calibration.* An image series using the experimental protocol was acquired, but with the EMCCD camera shutter closed. EMCCD offset, gain, and readout noise were estimated by fitting a statistical model suitable for low light intensity (one or zero photons per pixel) to the image series. These images mainly consist of electronic readout noise plus occasional photons generated spontaneously on the EMCCD camera chip and electron-multiplied just like normal photoelectrons. Under the assumption that this dark current is low enough to generate at most one photon per frame and pixel, this leads to a pixel intensity distribution with a more tractable form than at higher intensity, and it also circumvents the experimental difficulty of generating a stable and even illumination. In particular, dark images were modeled with a mixture model, where the value $c_{i,t}$ of pixel i at time t is modeled as:

$$c_{i,t} = o_i + \xi_{i,t} + s_{i,t} \cdot m_{i,t}$$

Here, o_i is a constant offset, $\xi_{i,t}$ are independent identically distributed (iid) Gaussian noise with zero mean and s.d. σ , $s_{i,t}$ are iid indicator variables that take values of 0 or 1 depending on whether a dark current electron was present or not, with $p(s_{i,t} = 1) = q$; $m_{i,t}$ models the electron multiplication noise of a single photoelectron by iid exponential variables with a mean value of $1/g$, where g is the effective EMCCD gain. A very similar approach was used by ref.⁵⁰; however, we explicitly include readout noise for the dark current photons ($s = 1$) as well but neglect spurious charges in the EM gain register. An expectation maximization algorithm was implemented to extract maximum-likelihood estimates of o_i , σ , q , and g from dark movies. The EM algorithm can be found as part of the uncertainSPT package¹⁸. At the light intensities (< 0.01 photons per pixel) and data sets (50–200 frames), the EMCCD gain parameter is usually recovered within a few percent.

Single-particle tracking. *Cell segmentation.* For practical reasons, fluorescence movies of colonies with no or very few fluorescent tRNAs (≤ 2 fluorophores per cell colony) were not included in the analysis. Cell outlines were extracted from phase contrast images using the algorithm in ref.⁵¹, and incorrectly segmented or dead (SYTOX stained) cells were manually removed. Alignment between segmented images and the fluorescence channel was done using landmarks in phase contrast and brightfield images. On a few occasions (≤ 2 cells per data set), cells with what appeared to be fluorescent impurities or unspecifically bound fluorophores completely immobilized for longer than 100 frames were omitted from the analysis.

Spot detection, localization, and trajectory building. Spots were detected using the radial symmetry-based method of ref.¹⁷, as implemented by <http://www.peterkovesi.com/matlabfns/Spatial/fastradial.m>. Spot positions and position uncertainty were estimated using a symmetric Gaussian spot model and the maximum a posteriori fit¹⁸, and trajectories were built using u-track¹⁹. We excluded spots > 3 pixels outside live cells, spots with width (std) > 280 nm, spots with amplitude < 50 photons, and spots in cells with > 2 spots. See Supplementary Note for details.

Mean square displacement plots. To extract mean-square-displacement (MSD)-based estimates of diffusion constants, trajectories were divided in segments of seven positions, an MSD curve was computed using x and y coordinates, and the apparent diffusion constant for that curve was estimated by a linear fit through the origin, i.e., $MSD(t) = 2dD\Delta t$, using the first two points ($t = 1, 2$) of the MSD curve for each segment. Here, $d = 2$ is the dimension of the trajectories, $\Delta t = 5$ ms is the time step, and the apparent diffusion constant D is the fit parameter. This neglects a small offset due to motion blur and localization errors⁵² but constrains the estimate of D to be non-negative.

Hidden Markov modeling. We used a diffusive HMM algorithm¹⁸ to analyze two-dimensional trajectories (motion in the z , y plane). This HMM fits ensembles of trajectories for each experimental condition to a global model, handles missing positions, and makes explicit use of positions as well as localization uncertainties of each position¹⁸. The algorithm was restarted with 100 independent initial values to find global maximum likelihood estimates (MLE) parameters, initial state probability, transition probabilities, and diffusion constants, for each considered model size. In addition, we used custom scripts to systematically prune states and build smaller models, similarly to the greedy search used by vbSPT³. We then used AIC²¹ to select the optimal model. Diffusion constants are estimated directly by the HMM maximum likelihood algorithm, as are posterior hidden state probabilities for each time step that we use to estimate overall occupancy. Mean dwell times were estimated from the diagonal of the maximum likelihood estimate of the HMM transition matrix, i.e., from the average probability of exiting a diffusive state. This mean dwell time estimate does not make use of dwell time histograms, and therefore works also when photobleaching and tracking difficulties produce trajectory lengths below the mean dwell time (Supplementary Fig. 5d), although an upward bias (probably due to the difficulty of detecting short events) is visible (Fig. 5c).

To condense an HMM with many states to an effective two-state description, and guard against the tendency for AIC to overfit HMM-like models¹⁸, the hidden states were classified as 'fast' or 'slow' using a threshold value of $1 \mu\text{m}^2/\text{s}$ (and 0.5 and $1.5 \mu\text{m}^2/\text{s}$ as a robustness control). Coarse-grained occupancies and diffusion constants were calculated as weighted averages, while coarse-grained mean dwell times were estimated from a coarse-grained transition matrix (for details, see the function `EMhmm.parameterEstimate` in the `uncertainSPT` suite, <https://github.com/bmelinden/uncertainSPT>).

For spatial occupancy plots, positions were classified as belonging to a certain (coarse-grained) hidden state if the HMM posterior probability was $> 95\%$, whereas more ambiguous positions were excluded.

EF-Tu-mEos2 tracking was performed similarly to [Cy5]tRNA with the following changes. A scale factor of 1.9 for gaussian kernel radii and a threshold of 6.5 for spot extraction were used in the dot detection step. Spots with spot amplitude < 200 photons were discarded. For trajectory building, the search radius was constrained to 800 nm (non-adaptive), and gaps of up to two missing positions were allowed.

Code availability. A scripted example of the pipeline for simulated data, including model and parameter files for SMEagol, is available in supplementary software

at the open research repository Zenodo (<http://zenodo.org>; <https://zenodo.org/record/1168228#.WuG1Ii5uaUk>).

The different parts of the image analysis pipeline, i.e., cell segmentation, spot detection, etc. were handled through custom written MATLAB scripts, available upon reasonable request.

Reporting Summary. Further information on experimental design is available in the Nature Research Reporting Summary linked to this article.

Data availability. The data and supplementary software that support the findings of this study is available at the open research repository Zenodo (<http://zenodo.org>; <https://zenodo.org/record/1168228#.WuG1Ii5uaUk>).

References

- Kurland, C.G., Hughes, D. & Ehrenberg, M. in *Escherichia coli and Salmonella: Cellular and Molecular Biology* (ed. Neidhardt, F.C.) (ASM Press, Washington, 1996).
- Schmidt, C. M., Shis, D. L., Nguyen-Huu, T. D. & Bennett, M. R. Stable maintenance of multiple plasmids in *E. coli* using a single selective marker. *ACS Synth. Biol.* **1**, 445–450 (2012).
- Tenson, T., Herrera, J. V., Kloss, P., Guarneros, G. & Mankin, A. S. Inhibition of translation and cell growth by minigene expression. *J. Bacteriol.* **181**, 1617–1622 (1999).
- Hanahan, D., Jessee, J. & Bloom, F. R. Plasmid transformation of *Escherichia coli* and other bacteria. *Methods Enzymol.* **204**, 63–113 (1991).
- Parthasarathy, R. Rapid, accurate particle tracking by calculation of radial symmetry centers. *Nat. Methods* **9**, 724–726 (2012).
- Harpsoe, K. B. W., Andersen, M. I. & Kjægaard, P. Bayesian photon counting with electron-multiplying charge coupled devices (EMCCDs). *Astron. Astrophys.* **537**, A50 (2012).
- Ranefall, P., Sadanandan, S.K. & Wählby, C. in *2016 IEEE 13th International Symposium on Biomedical Imaging (ISBI)*. 205–208 (IEEE, 2016).
- Vestergaard, C. L., Blainey, P. C. & Flyvbjerg, H. Optimal estimation of diffusion coefficients from single-particle trajectories. *Phys. Rev. E* **89**, 022726 (2014).

Life Sciences Reporting Summary

Nature Research wishes to improve the reproducibility of the work that we publish. This form is intended for publication with all accepted life science papers and provides structure for consistency and transparency in reporting. Every life science submission will use this form; some list items might not apply to an individual manuscript, but all fields must be completed for clarity.

For further information on the points included in this form, see [Reporting Life Sciences Research](#). For further information on Nature Research policies, including our [data availability policy](#), see [Authors & Referees](#) and the [Editorial Policy Checklist](#).

► Experimental design

1. Sample size

Describe how sample size was determined.

The sample size for tracking data is denoted in total number of trajectory steps (n) and specified for each dataset (in figure legends and Supplementary Table 1). Number n is typically more than 8000 and was chosen such that Hidden Markov Model analysis of the dataset converges with acceptable errors as described in more detail in “Simulated microscopy data validates the analysis pipeline” section of the manuscript. To reach the desired number n , experiments were reproduced in several replicas (exact is specified in Supplementary Table 1). Typically, each replica of single-molecule microscopy experiment comprises tracking of molecules in 10-100 cell colonies with internalized [Cy5]tRNA.

2. Data exclusions

Describe any data exclusions.

For practical reasons, fluorescence movies of colonies with no or very few fluorescent tRNAs (≤ 2 fluorophores per cell colony) were not included in the analysis. Cy5 fluorescence data from dead cells (based on SYTOX staining), cells not completely covered in the field of view (i.e. half cells etc), and incorrectly segmented cells (with obvious deviation from cell outline based on visual inspection) were omitted from the analysis. On a few occasions (≤ 2 cells per dataset), cells with what appeared to be fluorescent impurities or unspecifically bound fluorophores, completely immobilized for longer than 100 frames, were omitted from the analysis.

3. Replication

Describe whether the experimental findings were reliably reproduced.

Each microscopy experiment was performed in 2–5 replicas (See Supplementary Table 1 for number of replicas) on different dates, generally using the same batches of electrocompetent cells and labeled tRNAs. The data was found consistent in between different repetitions (for example, see Supplementary Figure 3d) and were combined for analysis to reach criteria for convergence of the Hidden Markov Model analysis (as described in the section “Sample size”). All attempts of replication were successful.

4. Randomization

Describe how samples/organisms/participants were allocated into experimental groups.

No experimental groups were used. Not relevant.

5. Blinding

Describe whether the investigators were blinded to group allocation during data collection and/or analysis.

The experimental setup was the same for all types of experiments, and the analysis of experimental data was performed automatically with the same parameters used in all sets of experiments. Hence, blinding is not relevant.

Note: all studies involving animals and/or human research participants must disclose whether blinding and randomization were used.

6. Statistical parameters

For all figures and tables that use statistical methods, confirm that the following items are present in relevant figure legends (or in the Methods section if additional space is needed).

- n/a Confirmed
- The exact sample size (n) for each experimental group/condition, given as a discrete number and unit of measurement (animals, litters, cultures, etc.)
 - A description of how samples were collected, noting whether measurements were taken from distinct samples or whether the same sample was measured repeatedly
 - A statement indicating how many times each experiment was replicated
 - The statistical test(s) used and whether they are one- or two-sided (note: only common tests should be described solely by name; more complex techniques should be described in the Methods section)
 - A description of any assumptions or corrections, such as an adjustment for multiple comparisons
 - The test results (e.g. P values) given as exact values whenever possible and with confidence intervals noted
 - A clear description of statistics including central tendency (e.g. median, mean) and variation (e.g. standard deviation, interquartile range)
 - Clearly defined error bars

See the web collection on [statistics for biologists](#) for further resources and guidance.

► Software

Policy information about [availability of computer code](#)

7. Software

Describe the software used to analyze the data in this study.

MagicPlot Pro 2.7.2 (Magicplot Systems, LLC), Origin 8 (OriginLab), MATLAB R2014a, R2015a, R2016a (MathWorks), uncertainSPT 0.9.2 (github.com/bmelinden/uncertainSPT), SMEagol 1.0.2 ([smeagol.sourceforge.net/](https://sourceforge.net/projects/smeagol)). For custom MATLAB scripts see "Code availability" in Online Methods.

For manuscripts utilizing custom algorithms or software that are central to the paper but not yet described in the published literature, software must be made available to editors and reviewers upon request. We strongly encourage code deposition in a community repository (e.g. GitHub). *Nature Methods* [guidance for providing algorithms and software for publication](#) provides further information on this topic.

► Materials and reagents

Policy information about [availability of materials](#)

8. Materials availability

Indicate whether there are restrictions on availability of unique materials or if these materials are only available for distribution by a for-profit company.

All unique materials used are readily available from the authors or from standard commercial sources

9. Antibodies

Describe the antibodies used and how they were validated for use in the system under study (i.e. assay and species).

No antibodies were used

10. Eukaryotic cell lines

a. State the source of each eukaryotic cell line used.

No eukaryotic cell lines were used

b. Describe the method of cell line authentication used.

No eukaryotic cell lines were used

c. Report whether the cell lines were tested for mycoplasma contamination.

No eukaryotic cell lines were used

d. If any of the cell lines used are listed in the database of commonly misidentified cell lines maintained by [ICLAC](#), provide a scientific rationale for their use.

No commonly misidentified cell lines were used

► Animals and human research participants

Policy information about [studies involving animals](#); when reporting animal research, follow the [ARRIVE guidelines](#)

11. Description of research animals

Provide details on animals and/or animal-derived materials used in the study.

No animals were used

Policy information about [studies involving human research participants](#)

12. Description of human research participants

Describe the covariate-relevant population characteristics of the human research participants.

The study did not involve human research participants